THE ASTRONOMICAL JOURNAL, 121:2524–2539, 2001 May
© 2001. The American Astronomical Society. All rights reserved. Printed in U.S.A.

CANDIDATE TIDAL DWARF GALAXIES ASSOCIATED WITH STEPHAN'S QUINTET

C. MENDES DE OLIVEIRA,[1] H. PLANA,[2,3] P. AMRAM,[3] C. BALKOWSKI,[4] AND M. BOLTE[5]

Received 2000 November 3; accepted 2000 December 27

ABSTRACT

We present kinematic and photometric evidence for the presence of seven candidate tidal dwarf galaxies in Stephan's Quintet. The central regions of the two most probable parent galaxies, NGC 7319 and NGC 7318B, contain little or no gas whereas the intragroup medium and, in particular, the optical tails that seem to be associated with NGC 7318B are rich in cold and ionized gas. Two tidal dwarf candidates may be located at the edge of a tidal tail, another located within a tail, and for the four others there is no obvious stellar/gaseous bridge between them and the parent galaxy. Two of the candidates are associated with H I clouds, one of which is, in addition, associated with a CO cloud. All seven regions have low continuum fluxes and high Hα luminosity densities [$F(\mathrm{H}\alpha) = (1\text{–}60) \times 10^{-14}$ ergs s^{-1} cm^{-2}]. Their magnitudes ($M_B = -16.1$ to -12.6), sizes ($\sim 3.5\ h_{75}^{-1}$ kpc), colors (typically $B-R = 0.7$), and gas velocity gradients ($\sim 8\text{–}26\ h_{75}$ km s^{-1} kpc^{-1}) are typical for tidal dwarf galaxies. In addition, the ratios between their star formation rates determined from Hα and from the *B*-band luminosity are typical of other tidal dwarf galaxies. The masses of the tidal dwarf galaxies in Stephan's Quintet range from $\sim 2 \times 10^8$ to $10^{10}\ M_\odot$, and the median value for their inferred mass-to-light ratios is 7 $(M/L)_\odot$. At least two of the systems may survive possible "fallbacks" or disruption by the parent galaxies and may already be, or turn into, self-gravitating dwarf galaxies, new members of the group.

Key words: dark matter — galaxies: dwarf — galaxies: interactions — galaxies: ISM — galaxies: kinematics and dynamics — intergalactic medium

1. INTRODUCTION

Optical and H I studies of interacting galaxies (e.g., Hibbard & van Gorkom 1996; Duc & Mirabel 1998) have shown that dwarf galaxies may be produced during galactic collisions. Duc & Mirabel (1998) have presented an especially convincing case for NGC 5291, where more than 10 star-forming high-metallicity dwarf galaxies may have been formed in a recent merger. These newly formed tidal dwarf galaxies may be good sites to study galaxy formation in the nearby universe.

Although the concept of the formation of self-gravitating objects in tidal tails is an old one, considered by Zwicky as early as 1956, it is only recently that these objects have received more attention and have been searched for systematically. H I observations have so far been the principal means used in searches for tidal dwarf galaxies, since these are usually gas-rich systems. H I maps can reach large radii but have the disadvantage of being (mostly) of too poor spatial resolution for a direct investigation of the velocity field of the spatially small, low velocity dispersion objects (typically 5″–20″ in extent, with velocity gradients of 2–20 km s^{-1} arcsec^{-1}; Duc 1995). The study of the kinematics of the *ionized* gas of a galaxy, when it is present, with high spatial and spectral resolution velocity maps can alternatively provide a useful tool to probe the nature of the candidate dwarf galaxies at small scales, complementing the lower resolution radio studies.

This paper presents new data on the kinematics of the ionized gas for seven star-forming tidal dwarf galaxy candidates and many other giant H II regions of Stephan's Quintet. Combining Fabry-Pérot Hα maps with deep *B* and *R* images, we study the photometric and kinematic properties of 23 emission-line regions of the group.

Stephan's Quintet (= Arp 319 = VV 288 = HCG 92) has been the subject of studies in X-rays, the radio continuum, H I, and Hα. Most of its gaseous material is concentrated not around the bright galaxies but in the intragroup medium, suggesting that collisions among the group members may have taken place. Arp (1973) was the first to obtain an Hα image of the group and to identify H II regions around galaxies NGC 7318AB, 7319, and 7320. As part of an imaging survey of compact groups, in the *R* band Hunsberger, Charlton, & Zaritsky (1996) identified 27 tidal dwarf galaxy candidates possibly associated with NGC 7318AB and NGC 7319. One of these regions was observed by Xu, Sulentic, & Tuffs (1999) to be a bright infrared source when observed with the *Infrared Space Observatory* (*ISO*) satellite (their source A). Xu et al. also presented Hα + [N II] images of the group highlighting the spatial overlap of two emission clouds of ionized gas in the intragroup medium, centered around 5700 and 6700 km s^{-1}. A similar result was found by Plana et al. (1999) based on Fabry-Pérot Hα maps.

An interesting possible scenario for the interaction history of Stephan's Quintet has been put forward by Shostak, Sullivan, & Allen (1984) and refined by Moles, Sulentic, & Márquez (1997) and Moles, Márquez, & Sulentic (1998). The scenario is based on the analysis of optical images of the Quintet, spectroscopy of a number of systems (Moles et al. 1998), and H I maps, which show three velocity components associated with the group, at ~5700, 6000, and 6700 km s^{-1} (Balkowski et al. 1973; Allen & Sullivan 1980; Shostak et al. 1984). In this scenario, one or more major

[1] Instituto Astronômico e Geofísico, Universidade de São Paulo, Avenida Miguel Stefano 4200, 04301-904 São Paulo, SP, Brazil.
[2] Observatorio Astronómico Nacional, Universidad Nacional Autónoma de México, Apdo. Postal 877, 22800 Ensenada, B.C., Mexico.
[3] Laboratoire d'Astrophysique de Marseille, Place Le Verrier 2, F-13248 Marseille Cedex 4, France.
[4] Département d'Astrophysique Extragalactique et de Cosmologie, Observatoire de Paris, CNRS and Université Paris 7, Place Jules Janssen 5, F-92195 Meudon Cedex, France.
[5] UCO/Lick Observatory, Board of Studies in Astronomy and Astrophysics, University of California, Santa Cruz, 1156 High Street, Santa Cruz, CA 95064.

collisions occurred between NGC 7320C and NGC 7319 (at velocities $\sim$6000 and $\sim$6700 km s^{-1}, respectively), which may have resulted in the removal of the H I gas from the inner parts of NGC 7319. More recently, Stephan's Quintet would have received a new member, NGC 7318B (it has a radial velocity of 5774 km s^{-1}, while the other core group members, NGC 7317, 7318A, and 7319, have a mean velocity of 6664 km s^{-1}; Hickson et al. 1992). NGC 7318B would be entering the group for the first time and would be colliding with the intragroup medium (Moles et al. 1997). We identify a number of possible tidal dwarf galaxy candidates, most probably formed as a result of the ongoing collision that involves NGC 7318B. Only one of the candidates studied here may be associated with the NGC 7320C–NGC 7319 collision and, hence, the H I cloud removed from the center of NGC 7319. An alternative possibility is that the latter originated from NGC 7318A (see §§ 4.7 and 4.8).

All the regions we measure in this work have been previously identified as H II regions by Arp (1973). A number of them have also been listed by Hunsberger et al. (1996) as tidal dwarf galaxy candidates, and by Gallagher et al. (2000, 2001, using *Hubble Space Telescope* images) as massive cluster candidates. However, these studies did not have velocity information. Radial velocity information for some of the regions is summarized in Table 1 of Plana et al. (1999). Determination of the velocity gradients within the regions is the main contribution of the present work.

The organization of this paper is as follows: Section 2 describes the observations and reduction procedure. In § 3, we present the new photometric and kinematic results. In § 4, we discuss the results, and § 5 summarizes. Throughout this paper, h_{75} is the Hubble constant in units of $H_0 = 75$ km s^{-1} Mpc^{-1}. We assume that all the regions are at the same distance and the differences in cz are just kinematic. For the figures and the determination of the star formation rates, we assumed a distance to the group of 80 Mpc, for an average velocity of 6000 km s^{-1} and a Hubble constant of 75 km s^{-1} Mpc^{-2}.

2. OBSERVATIONS AND DATA REDUCTION

2.1. *Fabry-Pérot Data*

The observations were carried out with scanning Fabry-Pérot instruments mounted on the 3.6 m Canada-France-Hawaii Telescope (CFHT) and the 6 m telescope of the Russian Special Astrophysical Observatory (SAO). The observations and characteristics of the setups are summarized in Table 1. During the CFHT run we mostly detected sources with radial velocities $V_R \sim 5700$ km s^{-1}, since we used a narrowband filter that cut the higher velocities. We therefore did not detect the 6700 km s^{-1} component of the group. The filter used during the observations at the SAO 6 m telescope allowed the detection of a much broader range of wavelengths, and both velocity components were detected. However, the data are of much lower signal-to-noise ratio (S/N) and spectral and spatial resolution than the CFHT data.

Reduction of the data was performed using the CIGALE/ADHOC software.[6] The data reduction procedure has been extensively described in Amram et al. (1995, 1996), Plana et al. (1998), and references therein.

Wavelength calibrations were obtained by scanning the narrow Ne 6599 Å line during the observations. The relative velocities with respect to the systemic velocities are very accurate, with an error of a fraction of a channel width (<3 km s^{-1}) over the whole field.

[6] See http://www-obs.cnrs-mrs.fr/adhoc/adhoc.html.

TABLE 1

FABRY-PÉROT OBSERVATIONS

Parameter	CFHT 3.6 m	SAO 6 m
Observations:		
Equipment	MOS/FP at Cassegrain	CIGALE at primary
Date	1996 Aug 23	1991 Aug 5
Seeing	$<1''$	$\sim 1''.2$
Interference filter:		
Central wavelength	6697 Å[a]	6726 Å[b]
FWHM	17 Å[a]	50 Å[b]
Transmission (maximum)	0.7[a]	0.55[b]
Calibration:		
Neon comparison light	6598.95 Å	6598.95 Å
Fabry-Pérot:		
Interference order	1162 at 6562.78 Å	796 at 6562.78 Å
Free spectral range at Hα	265 km s^{-1}	380 km s^{-1}
Finesse at Hα	12	12
Spectral resolution at Hα	27344 at the sample step	18750
Sampling:		
Number of scanning steps	24	24
Sampling step	0.24 Å (11 km s^{-1})	0.35 Å (16 km s^{-1})
Total field	$440'' \times 440''$ (512 × 512 pixels)	$170'' \times 170''$ (256 × 256 pixels)
Pixel size	$0''.86$	$0''.67$
Detector	STIS2 CCD	IPCS
Exposures times:		
Total exposure time	1.2 hr	0.8 hr
Each scanning exposure time	180 s	20 s per channel
Total exposure time per channel	180 s	120 s

[a] For a mean beam inclination of 2°.7.
[b] For a mean beam inclination of 5°.3.

The signal measured along the scanning sequence was separated into two parts: (1) a constant level produced by the continuum light in a narrow passband around Hα (continuum map), and (2) a varying part produced by the Hα line (monochromatic map). The continuum level was taken to be the mean of the three faintest channels. The monochromatic map was obtained by integrating the monochromatic profile in each pixel.

The CFHT data were roughly calibrated in flux by using a common galaxy also observed in a previous run when a flux calibrator was observed (Amram et al. 1998). We estimate an error of 30% in the flux calibration. The Hα profiles were measured to a minimum flux density of 4.9×10^{-17} ergs s^{-1} cm^{-2} $arcsec^{-2}$. We were not able to flux-calibrate the data obtained at the SAO 6 m telescope, for lack of calibrators.

2.2. *Imaging*

Images of Stephan's Quintet in B (5×900 s) and R (6×350 s) were obtained with the CFHT and the Subarcsecond Imaging Spectrograph. The values of seeing on the final images were 0.″8 and 0.″6, respectively.

Preprocessing of all frames through flat-fielding was carried out using IRAF tasks. The individual frames were registered and combined with a clipping scheme that eliminated the one lowest and one highest pixel value in each registered stack to exclude cosmic rays, hot pixels, and low pixels.

The program SExtractor (Bertin & Arnouts 1996) was used to obtain photometry of all objects in the B and R images with a sky "mesh size" of 128 pixels. "Automatic aperture magnitudes" were obtained, which give total magnitudes for the objects (based on Kron's 1980 first-moment algorithm).

Calibration to the standard system for the B- and R-band observations was accomplished via observations of standard stars from the list of Landolt (1992) and updated magnitudes for the KPNO consortium fields in M92 and NGC 7006. The transformations from instrumental to standard systems were made using the following: $R = r + 0.015(B-R) + 31.37$ and $B = b + 0.047(B-R) + 31.27$. The final combined images of HCG 92 can be obtained upon request. A $B-R$ map was obtained after the images were calibrated and their seeing profiles were matched (shown in Fig. 1*a*).

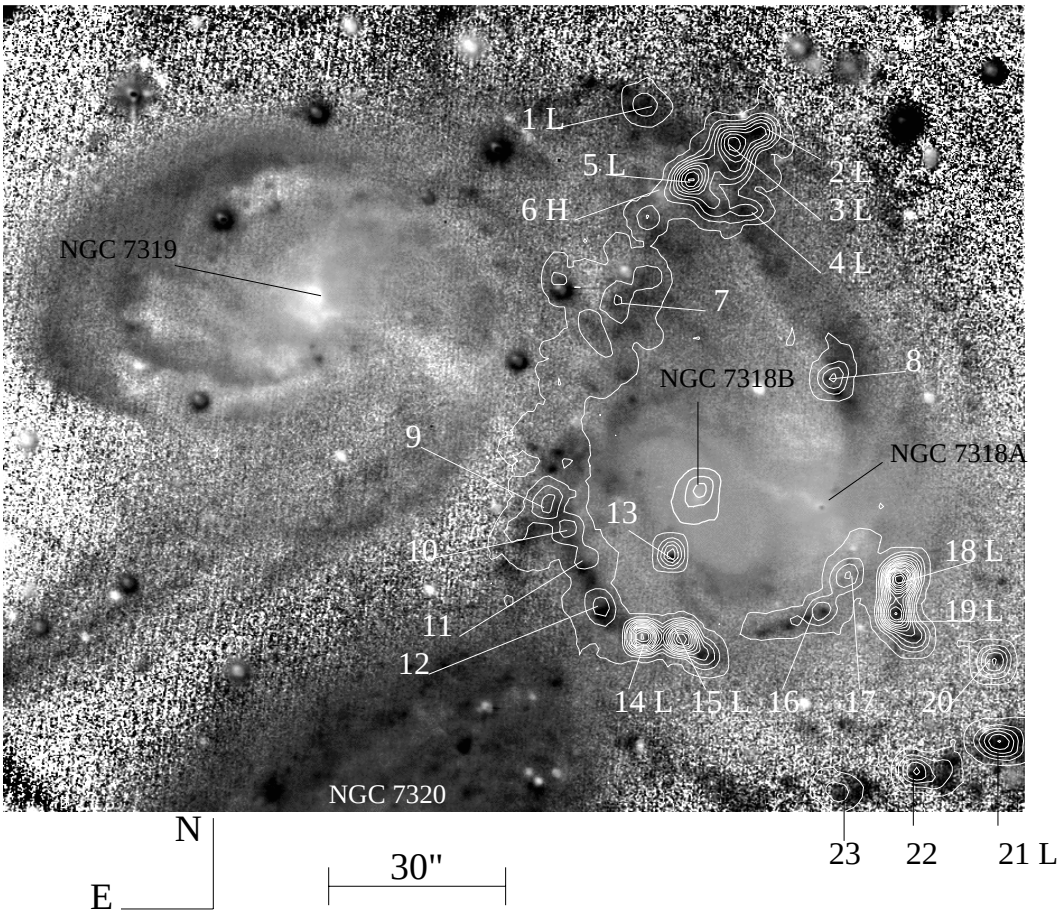


FIG. 1*a*

FIG. 1.—(*a*) $B - R$ color image. Dark is blue and white is red. The dimensions of the image are $3' \times 2'.4$, and north is up and east is to the left. The Hα monochromatic emission contours are shown, and the 23 emitting regions detected by Plana et al. (1999) are marked. An "L" (for low) marks regions known to have velocities in the range 5700–6000 km s^{-1}, while an "H" (for high) marks region 6, the only region for which the velocity is confirmed to be ~6700 km s^{-1}. The monochromatic contours are flux-calibrated. The lowest level is 4.2×10^{-17} ergs s^{-1} cm^{-2} $arcsec^{-2}$, and the step is 1.7×10^{-17} ergs s^{-1} cm^{-2} $arcsec^{-2}$. (*b*) R image of the group after sky subtraction. Optical blobs corresponding to Hα-emitting regions are marked. (*c*) Final combined B image of the Quintet. Linear features that could possibly be associated with NGC 7318A are marked with arrows.

3. RESULTS

3.1. *Magnitudes and Colors of the Emission-Line Regions*

The Hα contours are shown superposed on the $B-R$ image of Stephan's Quintet in Figure 1*a*. The 23 emitting regions detected by Plana et al. (1999) are marked. Dark is blue and white is red. The letters "L" and "H" are used to identify the systems for which we have an unambiguous determination of the radial velocity. Those marked "L" belong to the low-velocity system associated with NGC 7318B, with velocities of 5700–6000 km s^{-1}, and the only system marked with "H," region 6, is the high-velocity system probably associated with NGC 7319, at a velocity of ~ 6700 km s^{-1}.

In Figure 1*b*, the corresponding *R* image of the group (after subtraction of a heavily smoothed sky) is shown. The optical blobs corresponding to the Hα-emitting regions are marked in this figure (e.g., regions 1A and 1B correspond to the *B* and *R* counterparts of region 1 in Hα; see Fig. 1*a*). All regions detected in Hα have counterparts on the *B* and *R* image. Region 17 is faint, it is affected by dust, and it is too close to the galaxy NGC 7318A. Although it is not evident given the contrast of Figure 1*b*, it does have a counterpart on the *B* and *R* images.

The $B-R$ image of the group shown in Figure 1*a* reveals some interesting features. The galaxy NGC 7319 may contain several dust spots (white regions in the figure, which are those with the reddest values of $B-R$); in particular, the one to the north of the galaxy corresponds to strong CO emission (Gao & Xu 2000). We also note that the center of NGC 7318A has a dust lane with a very peculiar shape, suggesting that this galaxy may have taken part in the interaction history of the group (not contemplated in the scenario described by Moles et al. 1997). The complicated dust lane structure of NGC 7318A is much more impressive in the *Hubble Space Telescope* (*HST*) public image of the group. Further evidence that galaxy NGC 7318A may be interacting is given by Figure 1*c*, which is discussed in § 4.7.

Table 2 shows the main photometric parameters for all 23 Hα-emitting regions shown in Figures 1*a* and 1*b* (with the exception of a few entries for region 17, for the reason explained above). Total *B* magnitudes ("automatic aperture magnitudes" given by SExtractor) and $B-R$ colors are listed in columns (2) and (4), respectively. When one Hα region corresponds to more than one identification on the *B* and *R* images, we list the apparent *B* magnitudes of the different blobs in a single entry, separated by slashes (magnitudes and colors are corrected for Galactic extinction only). The $B-R$ color was measured inside an aperture of 1.″0 radius centered on each blob. The total absolute magnitudes given in column (3) correspond to the sums of the individual luminosities (e.g., the absolute magnitude for region 8 [see Fig. 1*a*] corresponds to the sum of regions 8A, 8B, and 8C [Fig. 1*b*]). The identifications footnoted "c" in

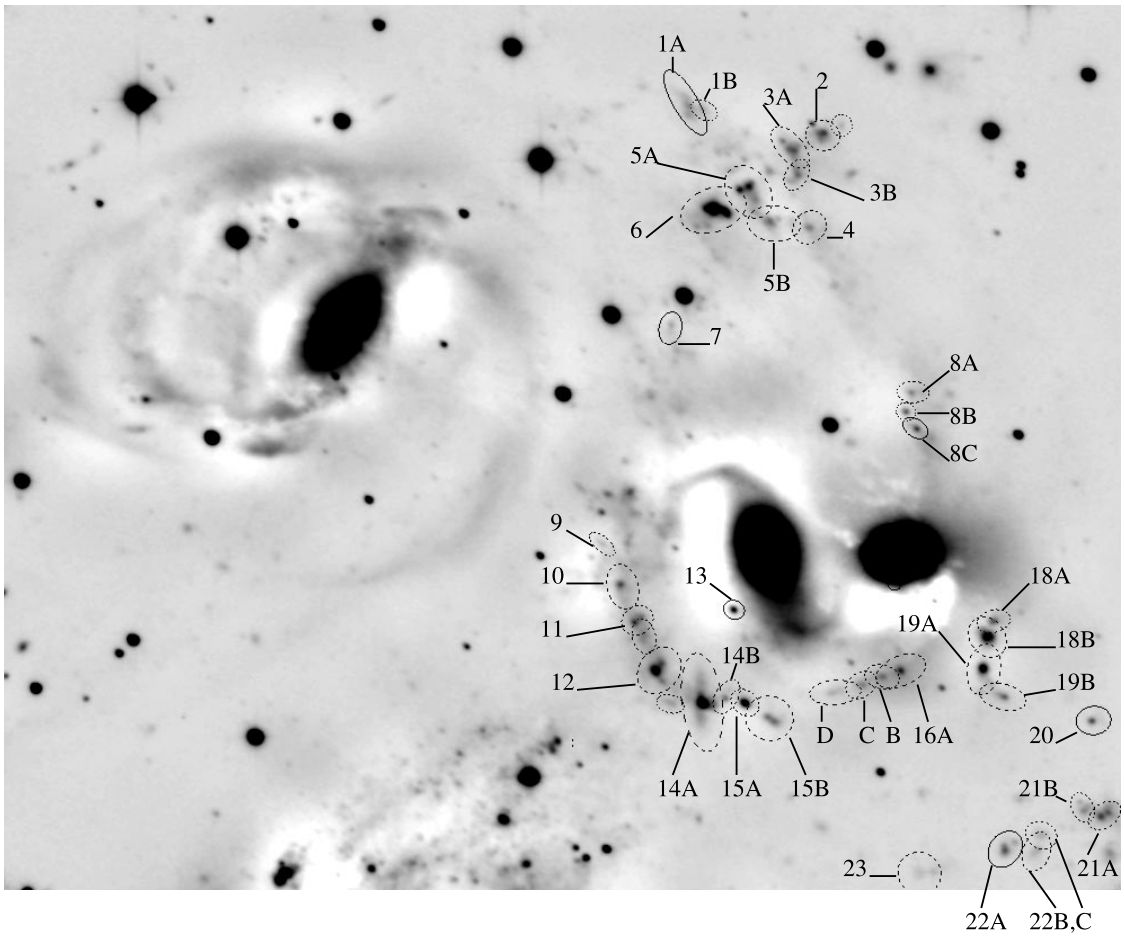


FIG. 1*b*

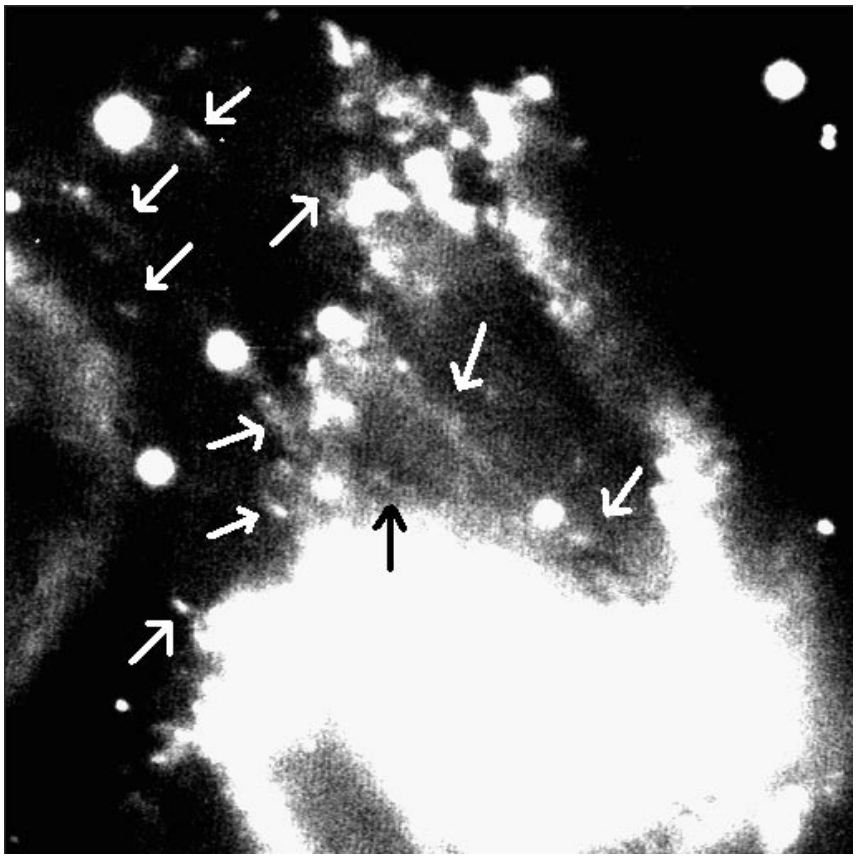


FIG. 1*c*

TABLE 2

PROPERTIES OF THE STAR-FORMING REGIONS OF STEPHAN'S QUINTET

ID (1)	B (mag) (2)	M_B (mag) (3)	$(B-R)_0$ (mag) (4)	Cont. (%) (5)	$F(\mathrm{H}\alpha)$[a] ($\times 10^{-14}$) (6)	SFR(Hα)[b] (7)	SFR(L_B)[b] ($\times 10^{-3}$) (8)	$a \times b$ (arcsec) (9)
1	20.7/21.9	−14.2	0.76	3.1	1.5	0.23	2.2	9.0 × 8.4
2[c]	20.6	−14.0	0.53	2.3	28.7	4.26	12.2	34 × 17
3[c]	20.3/20.9	−14.7	0.55	3.3	...	...		
4[c]	21.2	−13.4	0.67	3.2	...	...		
5[c]	19.6/20.7	−15.3	0.47	3.9	...	...		
6[c]	19.5	−15.0	1.32	3.6	...	...	4.5	16.0 × 13.0
7	21.5	−13.0	0.75	3.2	0.3	0.04	0.7	2.6 × 3.4
8[c]	21.4/22.3/21.2	−14.2	0.79	3.0	2.5	0.38	2.2	13.7 × 7.5
9	23.2	−11.4	1.00	...	2.5	0.38	0.2	7.4 × 4.6
10.....	20.1	−14.5	0.92	6.3	0.7	0.09	2.9	3.1 × 3.1
11.....	20.8	−13.7	0.58	4.8	0.7	0.09	1.4	4.7 × 3.1
12.....	19.6	−4.9	0.43	4.6	0.7	0.10	4.1	8.3 × 4.8
13.....	21.5	−13.0	0.77	...	2.2	0.32	0.7	8.6 × 5.6
14[d].....	19.3/21.2	−15.4	0.94	6.3	8.1	1.20	6.5	9.2 × 6.7
15.....	20.8/20.4	−14.7	1.00	4.7	9.6	1.42	3.4	10.8 × 9.3
16.....	21.1/21.6/22.0/21.5	−14.3	0.86	5.4	3.2	0.46	2.4	3.3 × 3.1
17.....	...	...	...	...	2.7	0.40	...	5.4 × 3.5
18.....	19.7/21.0	−15.1	0.56	4.0	13.4	2.00	4.9	11.9 × 9.0
19.....	20.3/21.5	−14.6	0.71	2.9	9.0	1.35	3.1	15.0 × 7.2
20[c].....	21.9	−12.6	0.76	0.3	3.0	0.45	0.5	10.5 × 8.0
21[c].....	20.1	−14.4	0.34	2.0	4.9	0.73	2.6	11.3 × 10.5
22[c].....	21.0/21.7/22.2	−14.2	0.42	1.0	4.2	0.63	2.2	11.8 × 9.7
23[c].....	21.5	−13.0	0.63	0.2	1.3	0.20	0.7	8.2 × 8.7

[a] In units of ergs s^{-1} cm^{-2}.
[b] In units of $M_\odot$ yr^{-1} $L_\odot^{-1}$.
[c] Object classified as a tidal dwarf galaxy.
[d] The magnitude and color of this region are contaminated by light from a red background galaxy.

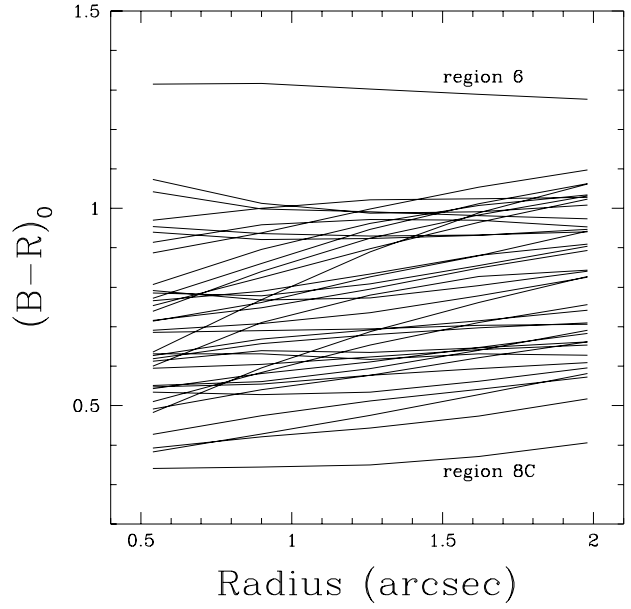


FIG. 2.—Corrected $B-R$ color gradient for each emission-line blob identified in Fig. 1*b*.

Table 2 correspond to the candidate tidal dwarf galaxies (see § 3.3). The magnitude and color of region 14A are contaminated by light from a red background galaxy that overlaps this region. There is an object to the northwest of region 2 that also seems to be a background object, given its red color.

We measure a very low continuum level (on the Fabry-Pérot map) for several of the Hα-emitting regions. Since we were not able to perform flux calibration of the continuum map (for lack of calibrators), we determined the ratio of the total flux contained in each blob to the flux within an arbitrary aperture of radius 1.″8 centered on galaxy NGC 7318B. This fraction is listed in column (5) of Table 2. This procedure is intended to show, in a relative way, which regions have the brightest and the faintest continuum emission. The regions with the lowest fluxes are regions 20 and 23. They have ~ 10 times less flux in the continuum than the median for the remaining regions. Regions 9, 13, and 17 could not be measured because of contamination from the bright galaxies NGC 7318A and 7318B.

We show color gradients for each emission-line blob in Figure 2. The $(B-R)_0$ (corrected for Galactic extinction) profiles in general become bluer toward each H II region, despite the fact that the *R*-band flux is contaminated by the Hα line emission. We can see from column (4) of Table 2 that all but one emitting region detected in Hα is blue (the median value of the color is 0.7). The exception is region 6, with a $B-R$ color of 1.3.

3.2. *Kinematics and Nature of the Emission-Line Regions*

Plana et al. (1999) detected 23 Hα-emitting regions around the NGC 7318AB system. For seven of them (six systems and one complex with four regions), a velocity field has been derived, shown in Figures 3*a*–3*g*. These correspond to the objects that show rotation. The velocity fields were used to derive the rotation curves shown in Figure 4. In all cases the velocities were measured within $\pm 35°$ of the major axis in the plane of the sky, except for regions 2–5 and 6, where a cone of $\pm 40°$ was used instead. The rotation curves were obtained using the position angle and inclination listed in columns (2) and (3) of Table 3. The position angle of the major axis (given in col. [2]) is taken to be the axis of symmetry of the main kinematic body of each galaxy. The center of the velocity field is, whenever possible, chosen to be a point along the major axis that makes the rotation curve symmetric, with similar amplitudes for the receding and approaching sides (this is however not always possible, e.g., region 6). The values of inclination with respect to the plane of the sky (given in col. [3]) are determined from the velocity fields of the candidates. Specifically, we used a least-squares fit program that gives the best value for the inclination while fixing the position angle, the central systemic velocity, and the kinematic center and fitting a classical rotation velocity model for data points inside annuli at increasing distances from the center.

In the top left panels of Figures 3*a*–3*g*, we show the Hα contours determined from the CFHT Fabry-Pérot maps, superposed on the deep *B*-band image of the galaxy (see also Plana et al. 1999). For region 6, the Hα map is derived from the SAO 6 m data (since its velocity was outside the filter range for the CFHT observations). The bottom left panels show the continuum-subtracted emission-line profiles. These have been smoothed spectrally, by a Gaussian function having a FWHM of three channels (or 35 km s^{-1}), and spatially (3 × 3 pixels), except for Figure 3*a* (see below). Each pixel represents 0.″86 on the sky. Although the pixel size for the image of region 6 was originally 0.″67, it was degraded to 0.″86 to match the CFHT data. In the right panels, we show the velocity fields of the galaxies superposed on the corresponding monochromatic Hα images. We mark the absolute value for each isovelocity for regions

TABLE 3

PHOTOMETRIC AND KINEMATIC PARAMETERS FOR THE TIDAL DWARF CANDIDATES

ID (1)	P.A. ± 5° (deg) (2)	Incl. (deg) (3)	L_B ($10^7\ L_\odot$) (4)	Rh_{75} (kpc) (5)	Dh_{75} (kpc) (6)	V_{max} (km s^{-1}) (7)	Mass ($10^8\ M_\odot$) (8)	Mass/L_B ($M_\odot/L_\odot$) (9)	M_{tid} ($10^8\ M_\odot$) (10)
2–5.....	125	55 ± 10	6.2	6.5	23	50	38	6	123
6	130	60 ± 15	2.7	3.5	24	50	20	7	12
8	−5	60 ± 5	1.9	4.5	13	115	138	73	225
20.....	70	65 ± 10	0.4	3.2	23	30	6.7	17	15
21.....	80	60 ± 5	1.4	3.5	27	55	24	17	12
22.....	75	55 ± 10	0.9	3.0	24	25	4.3	5	11
23.....	40	50 ± 10	0.4	2.0	23	23	2.4	6	3.6

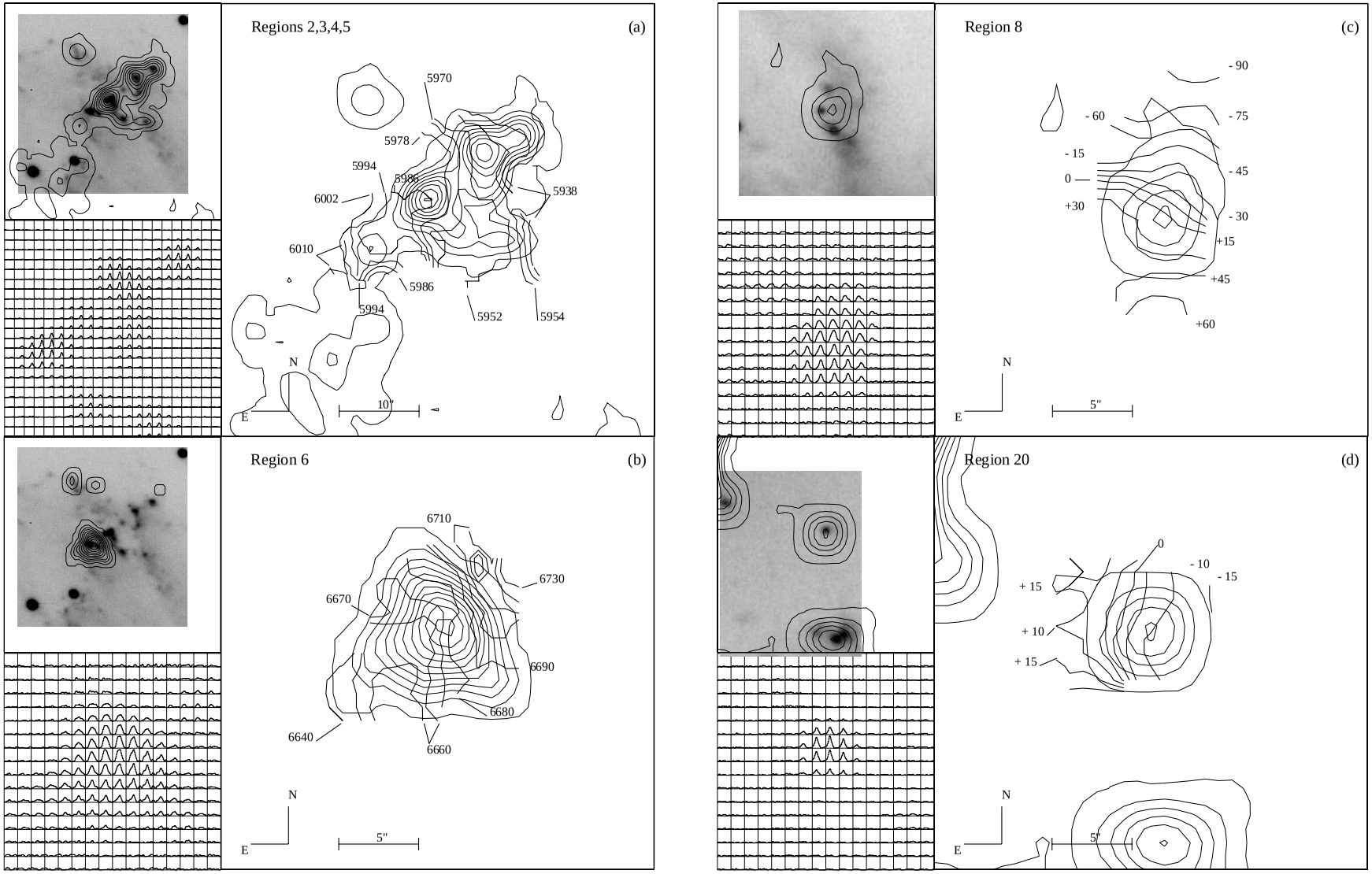
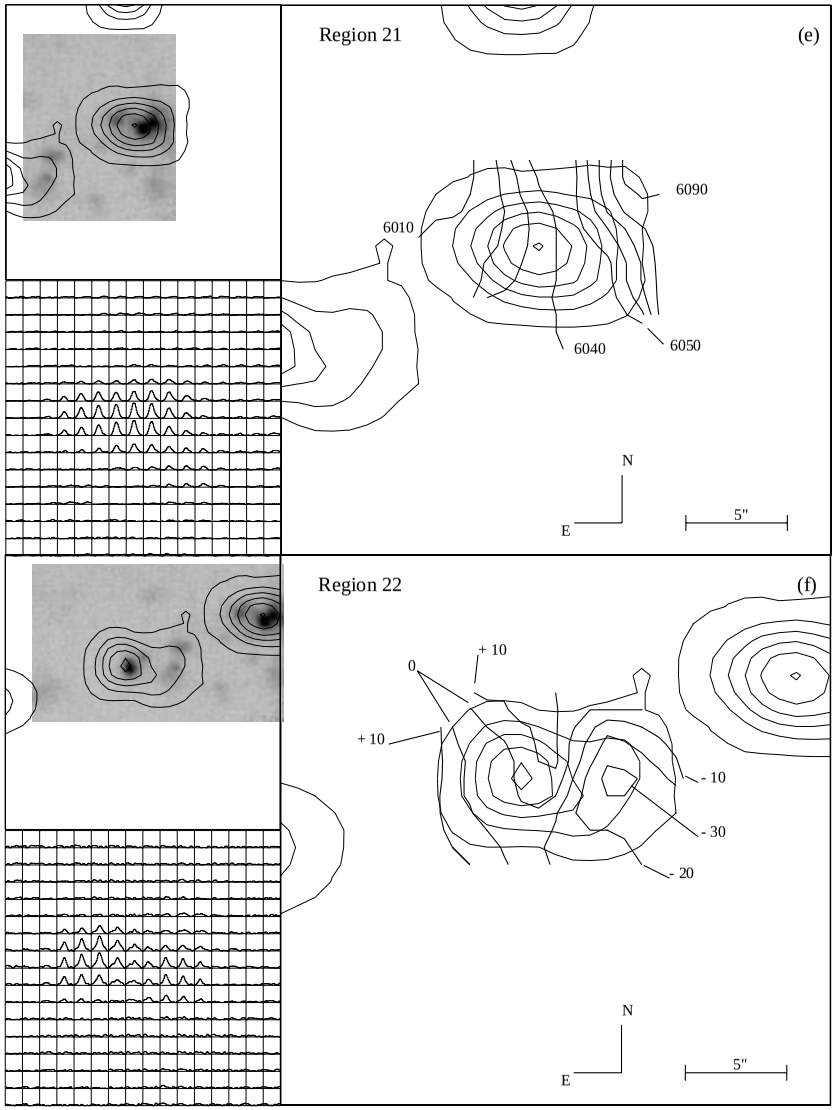


FIG. 3.—(*a–g*) *Top left*, *B*-band image superposed on the monochromatic map, with the isocontours the same as those presented in Fig. 1*a*; *bottom left*, profiles from the Fabry-Pérot data cube—the pixel size is 0.″86; *right*, the velocity field superposed on the monochromatic image. The field size for the right panel is the same as that for the top left panel.



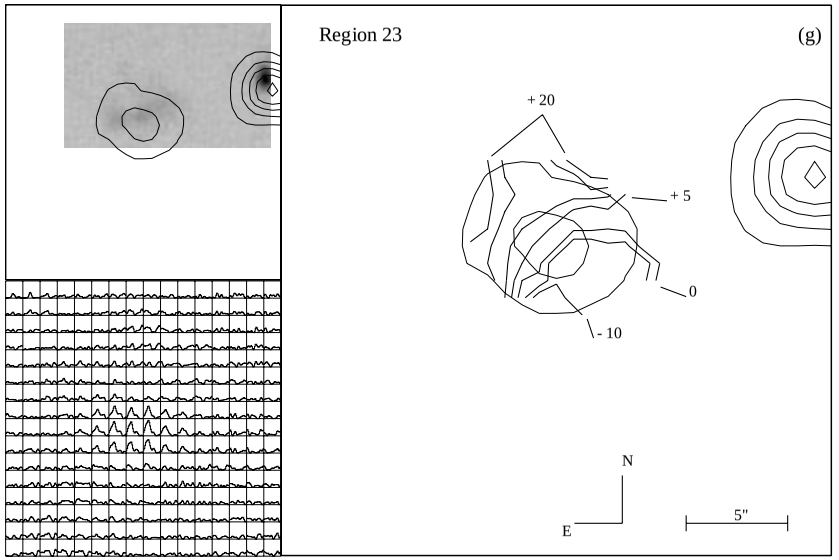


FIG. 3.—*Continued*

2–5, 6, and 21, but for regions 8, 20, 22, and 23, only relative velocities are marked, since we do not know the systemic velocities of these regions.

We classify systems 2–5, 6, 8, 20, 21, 22, and 23 as tidal dwarf galaxy candidates on the basis of the clear signature of rotation, above a cutoff value of 8.0 h_{75} km s^{-1} kpc^{-1}. Examples of nonrotating structures, possible associations of giant H II regions, are regions 9, 10, 11, 14, 15, 18, and 19.

We see continuous profiles between regions 9 to 11 (the data have S/N > 20 between the emission blobs), showing that these are connected. These regions are most probably attached to the southern tail of NGC 7318B. No velocity gradients are detected within them. Regions 14 and 15 are attached to one or more tidal tails (these regions correspond to double velocity components; Plana et al. 1999). Even if these complexes have Hα fluxes, sizes, and colors consistent with their being tidal dwarf galaxies (like the ones studied by Duc 1995), we detect no velocity gradient within the objects. In the same way, regions 18 and 19 also show bright Hα emission with no velocity gradients. These are very close to NGC 7318A, but as indicated by their radial velocities (∼5700 km s^{-1}; Plana et al. 1999), they may belong to NGC 7318B. Regions 18 and 19 do not have any obvious contact with a tidal arm.

Region 1 is isolated. We detected no velocity gradient within the region, but the S/N of the data may be too low to allow a gradient measurement. We summarize below the properties of each object that we classify as a candidate tidal dwarf galaxy.

3.3. *Properties of the Candidate Tidal Dwarf Galaxies*

Regions 2–5.—The complex formed by regions 2–5 has a radial velocity of 6020 km s^{-1} (velocity obtained by Moles et al. 1998 for region 2), and it shows an Hα diameter (full width at zero intensity) of ∼34″ (corresponding to a radius of $R = 6.5\ h_{75}^{-1}$ kpc). In order to increase the S/N, we performed a spatial smoothing of 3 × 3 pixels in the center and 5 × 5 pixels outside the inner region. Since this complex is large, smoothing does not affect the results. We can see in the bottom left panel of Figure 3*a* that the complex formed by regions 2–5 is connected by continuous velocity profiles. Although with a much lower S/N, the effect is also measurable in the unbinned data. This suggested to us that these regions may form one system, perhaps within a tidal tail. Figure 4*a* shows the corresponding rotation curve. The approaching and receding sides of the rotation curve differ in shape and amplitude. The curve is increasing regularly, reaching an average maximum velocity of 50 km s^{-1}. As the monochromatic map shows, we have at least four emitting regions, and therefore the velocity field and rotation curve may be averages of internal motions of these various regions. This could explain, at least partially, the disturbances of the velocity field. The *R* image in Figure 1*b* shows at least six bright condensations. The system as a whole has no defined center. The conditions needed for the complex of regions 2–5 to become an independent galaxy are discussed in §§ 4.1 and 4.6. We conclude that there is little chance that this region will survive as a single object. It could, however, form several condensations that could then be stable. We point out that there is an H I cloud encompassing the region with velocity similar to the optical velocity measured from the Hα emission (∼6000 km s^{-1}; Williams et al. 1999).

Region 6.—This region has a radial velocity of 6680 km s^{-1} (Moles et al. 1998). It shows a disturbed and fairly extended velocity curve out to a radius of $R = 3.5\ h_{75}^{-1}$ kpc. The profiles shown in the bottom left panel of Figure 3*b* indicate a larger velocity dispersion (i.e., they have larger widths) than for the other regions (∼115 km s^{-1} compared with 80 km s^{-1} for the others). A larger dispersion is expected when there is, for example, a second component blended with the main velocity component. However, in the case of region 6 the components are not resolved, and any attempt to decompose them would be arbitrary. As can be seen in Figure 3*b*, some of the profiles do show double peaks, but no consistent solution for a moving second component could be found, perhaps because of low S/N. The rotation curve presented in Figure 4*b* is peculiar. There is complete disagreement between the amplitudes of the receding and the approaching sides. The approaching side has approximately constant velocity at ∼10 km s^{-1}, while for the receding side the velocity reaches 90 km s^{-1}. The maximum rotational velocity listed in Table 3 is taken to be the average between both sides. The mass estimate obtained from this number is therefore very uncertain. Williams et al. (1999) have detected an H I cloud at the position of region 6 with similar velocity to that measured from the Hα emission (∼6700 km s^{-1}). It was also detected in CO by Gao & Xu (2000). In addition, this region was detected with *ISO* by Xu et al. (1999) and was found to be a very bright source in the infrared. This could therefore be a peculiar object, given its infrared luminosity and its disturbed rotation curve.

Region 8.—This region shows an extent of $R \sim 4.5\ h_{75}^{-1}$ kpc. The velocity field is quite regular. Figure 4*c* shows the rotation curve rising up to an average maximum velocity of 115 km s^{-1} in 12″ (∼4.5 h_{75}^{-1} kpc). This is the largest maximum rotational velocity we detect for a candidate tidal dwarf galaxy. Interestingly enough, this is the only tidal dwarf galaxy that seems to be embedded in a tidal tail, and it is the one closest to the parent galaxy. Nonetheless, the very high velocity gradient measured along a very short path and the optical condensations coincident with the emission-line region motivated us to list this as a possible candidate.

Region 20.—This region has an extent of $R \sim 3.2\ h_{75}^{-1}$ kpc. As the profiles of Figure 3*d* show, the emission is centrally concentrated. The rotation curve presented in Figure 4*d* is regular except outside a radius of $2\ h_{75}^{-1}$ kpc, where we can see a discrepancy between the approaching and the receding sides. The average maximum velocity is 30 km s^{-1}. The *R* image in Figure 1*b* shows a single center and no bridge to the parent galaxy (possibly NGC 7318B).

Region 21.—This region has an extent of $R \sim 3.5\ h_{75}^{-1}$ kpc. The velocity field (Fig. 3*e*) does not show perturbed isovelocities, but the position angle changes along the radius. The rotation curve, shown in Figure 4*e*, is derived along a mean position angle of the major axis of ∼80°. The approaching side of the rotation curve has a normal behavior, with velocities increasing up to 65 km s^{-1}. For the receding side, because of the position angle change, the velocities are scattered beyond $2\ h_{75}^{-1}$ kpc. The *R* image in Figure 1*b* shows two condensations, the westernmost being the brightest.

Region 22.—This region shows an extent of $R \sim 3\ h_{75}^{-1}$ kpc. The velocity field is disturbed. A second component may also be present in this case, as suggested by the profiles of Figure 3*f*. We were not able, however, to obtain a satis-

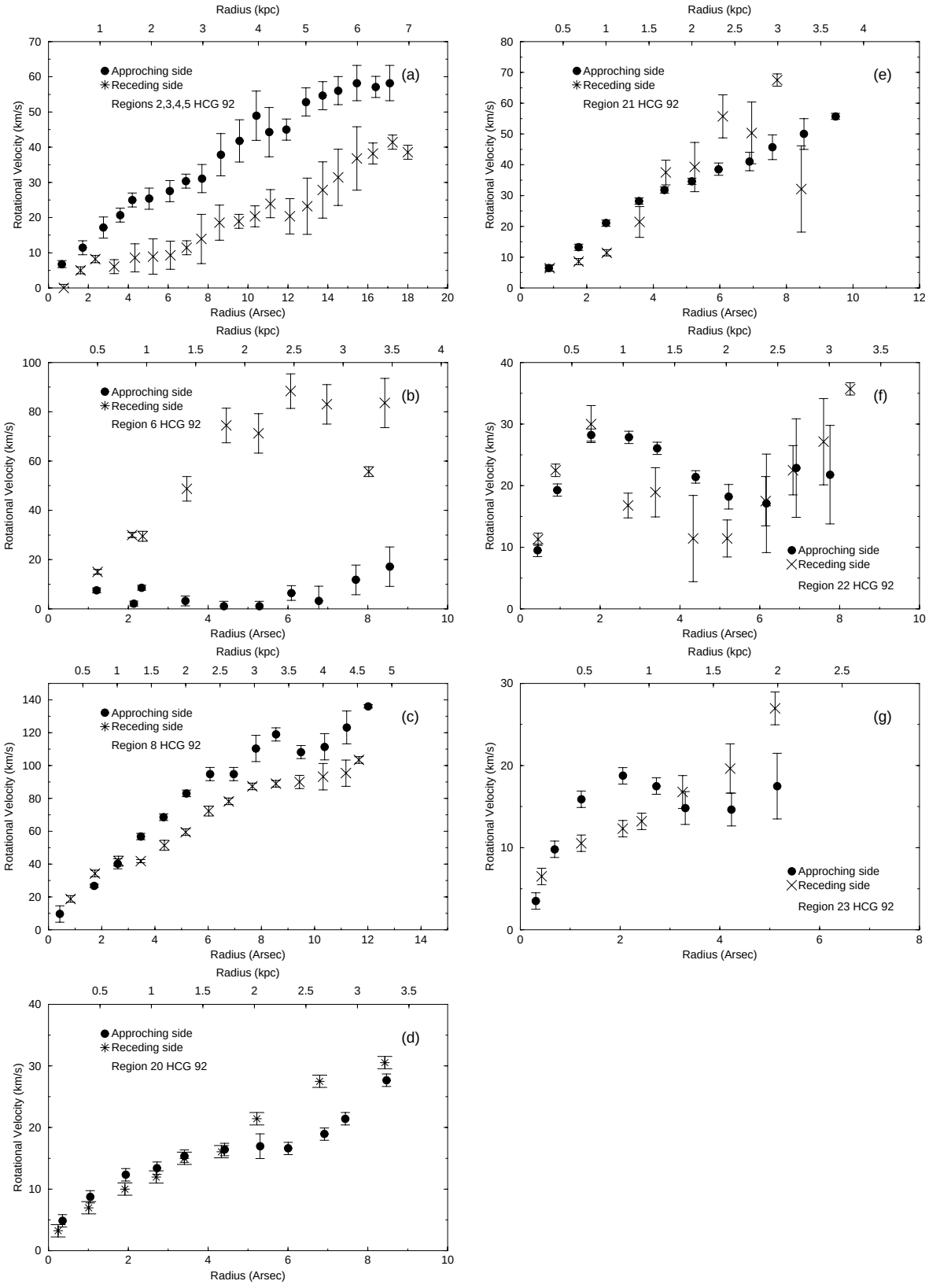


FIG. 4.—Rotation curves of the seven candidate dwarf galaxies. The parameters of the rotation curves are given in Table 3.

TABLE 4

SUMMARY OF THE PROPERTIES OF THE TIDAL DWARF GALAXIES

ID (1)	Blue Color (2)	SFR(Hα)/SFR(L_B) Condition (3)	Velocity Gradient Condition (4)	M_{tid} (5)	V_{esc} Condition (6)	Location (7)	Associated with H I Cloud? (8)
2–5.....	+	+	+	−	−	End of tail	+
6	−	+	+	+	−	End of tail	+
8	+	+	+	−	−	Inside a tail	−
20	+	+	+	−	−	Isolated	−
21	+	+	+	+	+	Isolated	−
22	+	+	+	−	+	Isolated	−
23	+	+	+	−	−	Isolated	−

factory decomposition of the two components. The rotation curve, shown in Figure 4*f*, presents a strong rise in the first 2″, a decrease in velocities after that, and then a new increase around $R \sim 6''$. The error bars are very large for radii beyond 6″, indicating a higher scatter in the velocities. Three condensations are seen in the optical image, the easternmost ones being the brightest. It is interesting to note that the blueshifted isovelocities of region 22 point toward the blueshifted isovelocities of region 21. This suggests that the velocity gradients measured are probably intrinsic to the regions and are not larger scale motions within a possible faint tidal tail that joins the regions.

Region 23.—This region has an extent of $R \sim 2\ h_{75}^{-1}$ kpc. The velocity field (Fig. 3*g*) does not show disturbed isovelocities, but the rotation curve (Fig. 4*g*) shows that the velocities for the approaching side increase in the first 2″ and then decline, while the velocities for the receding side increase with radius. The receding and the approaching sides are therefore not in agreement.

The rotation curves for four of the galaxies rise linearly with radius, without reaching a significant plateau. For two dwarf galaxy candidates, regions 22 and 23, the shape of the curve is disturbed. For region 6, the shapes of the approaching and receding sides are very different.

The rotation curves presented here can be compared with those for other tidal dwarf galaxies and blue compact galaxies. This is done in § 4.2.

3.4. Hα *Luminosities and SFRs*

Table 2 gives Hα fluxes for each emitting region, derived from the calibrated monochromatic map, measured above a threshold of 4.9×10^{-17} ergs s^{-1} cm^{-2} arcsec^{-2}, within apertures of diameters given in column (9) (defined as the diameter of the aperture of zero intensity). For region 6 no flux is listed, given that the data for this region are uncalibrated (see § 2.1).

The current star formation rate can be derived from the formula $\mathrm{SFR(H}\alpha) = 7.5 \times 10^{-8} L_{\mathrm{H}\alpha}$ ($M_\odot$ yr^{-1} $L_\odot^{-1}$). This formula is valid for 0.1–100 $M_\odot$ (Hunter & Gallagher 1986). The Hα fluxes given in column (6) of Table 2 were transformed to luminosities for use in the formula above by integrating over a sphere of space, assuming spherical geometry and a distance to the group of 80 Mpc.

In contrast to the Hα luminosity, the *B* luminosity is more sensitive to the older stellar population of a system (Larson & Tinsley 1978). Using the formula proposed by Gallagher, Hunter, & Tutukov (1984), it is possible to derive the star formation rate averaged for a period of 10^9 yr: $\mathrm{SFR}(L_B) = 0.29 \times 10^{-10} L_B$ ($M_\odot$ yr^{-1} $L_\odot^{-1}$). The ratio $\mathrm{SFR}(L_B)/\mathrm{SFR}(L_{\mathrm{H}\alpha})$ gives a rough measure of the evolution of the star formation rate inside the emission-line region during the last gigayear. The star formation rates are listed in columns (7) and (8) of Table 2 and are discussed in § 4.3.

4. DISCUSSION

4.1. *Masses, Mass-to-Light Ratios, and Escape Velocities*

The fate of a tidal dwarf galaxy is basically driven by the ratio of its mass to the virial mass and the ratio of its mass to the so-called tidal mass (Binney & Tremaine 1987; Duc 1995). The virial mass condition tells us whether the tidal dwarf candidate is massive enough to be gravitationally stable against internal motions. The tidal mass condition will tell us whether it is massive enough to survive the tidal forces exerted by the parent galaxy. In this work we only estimate the tidal mass, since for the virial mass we would need a measurement of the internal velocity dispersion of the galaxy, which we do not have.

In Table 3 we give, for each dwarf galaxy candidate, (1) the region identification number, (2) the position angle, (3) the inclination, (4) the total luminosity of the region in the *B* band, measured inside an aperture of size similar to that within which the ionized gas was measured, (5) the radius *R* that corresponds to the maximum rotational velocity (except for region 22, where *R* is the radius within which emission was detected), (6) the distance to the parent galaxy, (7) the maximum rotational velocity (derived from the rotation curves, shown in Fig. 4), (8) the total galaxy mass, (9) the mass-to-light ratio, and (10) the tidal mass.

The values given in columns (6), (8), and (10) are based on the following assumptions: (*a*) the tidal dwarf galaxy candidate was drawn from material from galaxy NGC 7318B (or NGC 7319 only for region 6), (*b*) the dwarf candidate presents a velocity gradient due to rotation, it is virialized, and therefore a value for the mass can be derived from the rotation curve, and (*c*) galaxies NGC 7319 and NGC 7318B have masses of 1.3×10^{11} and 1.8×10^{11} $M_\odot$, respectively (see below).

Total masses of the tidal dwarf galaxy candidates.—We estimated the total mass of the candidate tidal dwarf galaxies from their rotation curves, derived from the velocity fields (Figs. 3*a*–3*f*) using the simple virial estimator in which the mass within a radius *R* of a rotating disk system is given by $M(R) = fRV(R)^2G^{-1}$ (Lequeux 1983). Here $V(R)$ is the rotational velocity at radius *R*, *G* is the gravitational con-

stant, and f is a constant value between 0.5 and 1. We chose a value of 1 for simplicity.

$M(R)$ is a lower limit on the estimate of the mass, since most likely these regions are not pure rotators. Random motions of the gas could provide significant dynamical support for the tidal dwarf galaxies, as indicated by their line widths. As an approximation, if we assume that the gas is in equilibrium and that the gas velocity ellipsoid is isotropic, a very rough estimate of the contribution from the pressure support could be made using an "asymmetric drift correction" following Oort (1965). For gaseous objects in formation, such as those present in Stephan's Quintet, and under the above assumptions, a general rule may be (1) for rotation curves with amplitudes $V_{\rm max} \sim 25$ km s^{-1}, i.e., for the most internal regions of the self-gravitating structures or for the least massive objects, the contributions from the dispersion and the rotation components may be comparable; (2) for $V_{\rm max} \sim 50$ km s^{-1}, the contribution of the dispersion velocity component may be approximately half that for the rotational velocity component; and (3) for $V_{\rm max} > 50$ km s^{-1}, i.e., at larger distances from the center of the objects and/or for more massive structures, the dispersion velocity may be negligible to first approximation.

M/L of the tidal dwarf galaxy candidates.—The mass-to-light ratios of the candidate dwarf galaxies were obtained by dividing the values in column (8) by those in column (4) of Table 3. The median value for the mass-to-light ratios of the tidal dwarf galaxy candidates is 7 $(M/L)_\odot$, with a large scatter, with values as high as 74 $(M/L)_\odot$ for region 8. The mass-to-light ratio of region 8 reflects its steep velocity gradient of $\sim 26\, h_{75}$ km s^{-1} kpc^{-1}, the highest among the tidal dwarf candidates observed (see discussion of this point in § 4.4).

Total masses of the progenitor galaxies.—In order to determine the tidal masses, an estimate of the total mass of the progenitor galaxies is necessary. As we were not able to measure the rotation curves of the parent galaxies NGC 7319 and NGC 7318B because of the lack of ionized gas in their disks, we estimated their masses using the Tully-Fisher relation ($M_B = -5.85 \log 2V_{\rm max} - 5.61$, Pierini 1999; the factor of 2 within the logarithm was included to match our definition of $V_{\rm max}$ to theirs). For absolute magnitudes of -21.4 and -21.3 and R_{25} of 10.4 and 13.2 h_{75} kpc for NGC 7319 and NGC 7318B, respectively, we obtain maximum velocities of 249 and 240 km s^{-1}. Using the virial estimator we then obtain masses of 1.3×10^{11} and $1.8 \times 10^{11}\, M_\odot$.

Tidal masses.—The tidal masses listed in column (10) of Table 3 were derived from Binney & Tremaine (1987), $M_{\rm tid} = 3M(R/D)^3$, where M is the mass of the parent galaxy, R is the radius of the tidal dwarf, and D is the distance to the parent galaxy. We assumed that the masses of the parent galaxies NGC 7318B (for regions 2–5, 8, 20, 21, 22, and 23) and NGC 7319 (for region 6) are 1.3×10^{11} and 1.8×10^{11} $M_\odot$, respectively, as calculated above. The results in Table 3 show that the dwarf masses determined are in two cases larger than the tidal masses (for regions 6 and 21), suggesting that the regions considered may survive tidal forces. This is not the case, however, for the complex of regions 2–5 and for regions 8, 20, and 22, for which the tidal mass is larger than the total mass estimated.

Escape velocities of the candidates.—We can also estimate the escape velocity of the tidal dwarf candidates and compare this velocity with the systemic velocity difference between the dwarf candidate and the parent galaxy. We have found that the velocity difference between region 21 and NGC 7318B is of the order of the escape velocity calculated at the distance of the region (27 h^{-1} kpc), indicating that it may be able to escape from the parent galaxy's potential. This is not the case for regions 2–5 and 6 (for the latter, NGC 7319 is the parent galaxy). For regions 8, 20, 22, and 23, we do not have a unique systemic velocity determination. Nevertheless, we can give some estimate based on the possible systemic velocities (see Plana et al. 1999). For these four regions (8, 20, 22, and 23), the minimum possible velocities are ~ 5935, 5855, 5975, and 5935 km s^{-1}, respectively (Plana et al. 1999, their Table 1). If we assume that NGC 7318B (with velocity 5774 km s^{-1}) is the parent galaxy, then the differences between the velocity of the parent galaxy and those for each of the tidal dwarf candidates are 161, 81, 201, and 161 km s^{-1} (or larger) for regions 8, 20, 22, and 23, respectively. On the other hand, the escape velocities are 344, 259, 253, and 259 km s^{-1}, respectively. Therefore, if the minimum possible velocities are the true radial velocities, only region 22 of the four may be able to escape the potential of the parent galaxy, since for this region the escape velocity is similar to the velocity difference. We then conclude that only two of the seven candidates may have velocities such that they can escape the gravitational field of the parent galaxy.

4.2. *Comparison of the Velocity Fields*

Just a few kinematic studies are available on tidal dwarf galaxies and dwarf galaxies in general. Duc & Mirabel (1998) showed velocity curves of dwarf galaxies around NGC 5291 measured from H I kinematics. The curves show in general stronger gradients than those measured for the galaxies in Stephan's Quintet. However, the diameters of the objects, as computed from the optical images, are similar.

Another set of velocity curves and rotation curves for dwarf galaxies comes from Östlin et al. (1999, 2000). Their sample is composed of luminous blue compact galaxies (BCGs). The radial extent of the rotation curves is comparable to those for the candidate tidal dwarf galaxies in Stephan's Quintet, and the velocity amplitudes also seem to be similar. The shapes of the rotation curves, however, are very different. While in our sample the rotation curves show in general a shape typical of solid-body rotation, in Östlin et al. (1999) the rotation curves of the BCGs have flat plateaus.

In Östlin et al. (1999, 2000), the velocity fields are irregular and often contain secondary dynamical components, although they in most cases display overall rotation. By comparison of the stellar masses (by means of multicolor images and spectral evolutionary synthesis analysis) with the total masses of the galaxies (derived from the rotation curves), they showed that at least half the galaxies cannot be supported by rotation. They found that the morphologies and dynamics of the BCGs suggest that the starburst activity in these galaxies is most likely triggered by mergers of dwarf galaxies, massive gas clouds, or both. It is possible that the candidate tidal dwarf galaxies are also partially supported by random motions as is the case for the BCGs. Moreover, the starburst activity in the tidal dwarf galaxies could also be nurtured by the merging of gas clouds during the ongoing tidal process.

Hunter, Hunsberger, & Roye (2000) have recently made a compilation of possible dwarf galaxies in many different

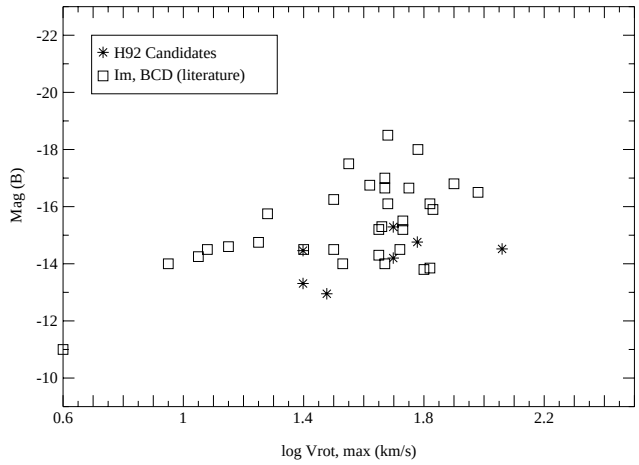


FIG. 5.—Maximum rotational velocity (corrected for inclination) vs. absolute *B* magnitude, for both the HCG 92 tidal dwarf candidates and a compilation of Im and blue compact dwarf galaxies from Hunter, Hunsberger, & Roye (2000).

environments that could be of tidal origin. A comparison of the maximum rotational velocities as a function of the absolute *B* magnitudes of the tidal dwarf galaxy candidates in Stephan's Quintet and galaxies in Hunter et al.'s sample is shown in Figure 5. As can be seen, the velocities and magnitudes of the HCG 92 tidal dwarf candidates are within the ranges of parameters of other possible candidates.

4.3. *Comparison of the SFRs for Various Classes of Emission-Line Objects*

There are several classes of emission-line objects that have similarities in some respects to the objects we observed in Stephan's Quintet. A comparison of the star formation rates for five samples of dwarf galaxies, one sample of H II regions in nearby spiral galaxies, and our sample is shown in Figure 6. We identified each of the galaxies in our sample with its corresponding identification number. Included in the comparison are (1) a sample of irregular galaxies from the Local Group (Mateo 1998), (2) a sample of isolated irregular galaxies of low luminosity and central surface densities, (3) a sample of blue compact galaxies studied by Sage et al. (1992) with blue luminosities similar to the systems

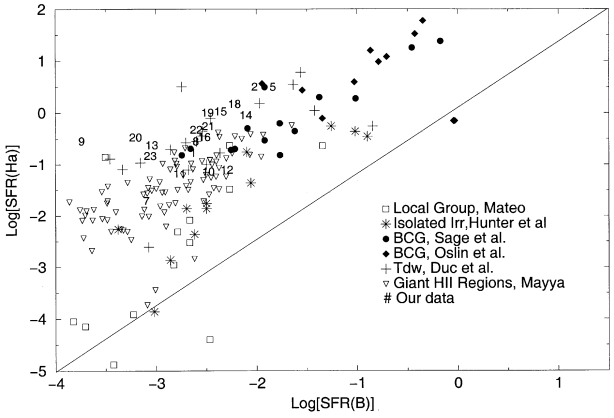


FIG. 6.—Current vs. recent star formation rates for several different classes of emission-line galaxies. The line corresponds to the locus where both measurements of the star formation rates are equal.

observed in Stephan's Quintet, (4) another sample of BCGs, studied by Östlin et al. (1999), (5) a sample of tidal dwarf galaxy candidates around NGC 5291 studied by Duc & Mirabel (1998), and (6) a sample of H II regions in the spiral galaxies NGC 1365, 1566, 2366, 2903, 2997, 3351, 4303, 4449, and 5253 studied by Mayya (1994, his Table 1; only objects with data quality 1 or 2 were included).

Figure 6 shows that the Local Group and isolated irregular galaxies have SFR(Hα) values that are on average lower than those for all the other samples. H II regions in nearby galaxies and BCGs have values of SFR(Hα) between those observed for isolated galaxies and those for tidal dwarf galaxies and giant H II regions of Stephan's Quintet. While in the sample of Sage et al. (1992) the BCGs have a comparable range of luminosities to the galaxies in the other samples, Östlin et al.'s sample is dominated by BCGs with high *B* luminosities. Still, the SFR(Hα)'s for these two samples agree in the region of overlap. The faintest BCGs seem to overlap with the location of the figure occupied by the H II regions in nearby spiral galaxies, although the latter extend to much lower luminosities. The tidal dwarf galaxies studied by Duc & Mirabel (1998) have average SFR(Hα)'s that are comparable to those of the objects studied in this paper. However, Duc & Mirabel's measurements were made through long-slit observations, and the values may be a lower limit on the Hα fluxes and, therefore, to the SFR(Hα)'s derived for these galaxies.

The SFR(Hα) values for the BCGs may be affected by dust, which would artificially lower the rates derived for these objects. Therefore, in reality the SFR(Hα)'s for tidal dwarf galaxies and BCGs may be similar although these galaxies are fundamentally two distinct classes (for instance, they have completely different metallicities, with the BCGs being metal-poor objects and the tidal dwarf galaxies having the high metallicities of their parent galaxies). One should also be aware that there exists a very large range of SFR(Hα)'s for both the BCGs and the tidal dwarf galaxies. Only a crude comparison between the SFR(Hα)'s of the two populations is thus possible.

4.4. *Considerations about Streaming Motions in Tidal Tails*

Region 8, as well as the complex of regions 2–5, seems to be a part of a tidal tail. In addition, region 6 may be at the edge of a tidal tail, if we assume that it is associated with NGC 7318A and not with NGC 7319 (see § 4.7). One obvious concern is then that the observed velocity gradients for these regions could be a result of streaming motion in the tail within which the region is embedded.

In the case of region 8, if we assume that it is attached to NGC 7318B (at a velocity of $\sim$5700 km s^{-1}) and has a velocity of $\sim$5900 km s^{-1} (J. Sulentic 1999, private communication), the gradient of the motion in the tidal tail (lower velocities in the south and higher velocities in the north) has the opposite sense to what is observed in the region itself (the red side of the region is to the south; see Fig. 3*c*). This represents clear evidence that the strong velocity gradient observed for region 8 cannot be due to streaming motions within the tidal tail. In addition, we note that there is a large misalignment of at least 30° between the position angle of the major axis of region 8 and that of the tidal tail within which it seems to be embedded (see Fig. 1*a*). This again indicates that region 8 cannot be just a part of a tidal tail and is, instead, an object with its own rotation pattern.

In the case of the complex of regions 2–5, we find that the velocity gradient we observed for it (these regions are located at the edge of a tidal tail that emanates from the northern arm of NGC 7318B) could not be strongly affected by streaming motions, for the following reason: For this complex we have information on the H I velocity field kindly provided by L. Verdes-Montenegro (2000, private communication). The motion observed in H I encompasses an area that goes from the base of the northern tail of NGC 7318B to our region 1, and it has a very similar mean radial velocity ($\sim$6000 km s^{-1}) to that of the Hα emission in complex 2–5. We compared the Hα and the H I velocity fields for regions 2–5 and found that while the Hα gradient reaches 50 km s^{-1} over a radius of 13″ in extent, the H I gradient reaches only about 15 km s^{-1} over the same area. Assuming that the H I velocity gradient gives us an upper limit on the large-scale motion of the tidal tail (an upper limit because some internal motion is also expected to be present in the H I component), the difference between the two gradients (35 km s^{-1}) is due to internal motions within the complex 2–5. With this correction, the new mass-to-light ratio of the complex of regions 2–5 would be 3 $(M/L)_{\odot}$.

In a scenario where region 6 was at the edge of the tidal tail that emanates from NGC 7318A, there would be no concern about its velocity gradient being due to streaming motion, since the center of the parent galaxy and region 6 have almost exactly the same velocity.

We conclude that streaming motions within the tails may not significantly change the observed velocity gradients measured in this study.

4.5. *Other Dynamical Considerations*

Dubinski, Mihos, & Hernquist (1999) find that a good criterion for making tidal tails during a collision appears to be that the ratio of the escape velocity ($V_{\rm esc}$) over the circular velocity ($V_{\rm max}$, in our notation) of the galaxy, measured at a radius of $2R_d$, must be lower than 2.5 (R_d is the scale length of the galaxy). According to Dubinski et al. (1999), this condition is valid for a wide range of models, including those with disk-dominated and halo-dominated rotation curves. They also find that galaxies with declining rotation curves are the best candidates to produce tidal tails during collisions. We do not have information on the rotation curves of the galaxies (as a consequence of their lack of ionized gas), but we can still check the velocity ratio condition $V_{\rm esc}/V_{\rm max} < 2.5$, assuming that the galaxies follow the Tully-Fisher relation (see § 4.1). The masses inside $2R_d$ are 1.1×10^{11} and 0.8×10^{11} $M_{\odot}$ for NGC 7318B and NGC 7319, respectively (if we assume that the scale length of the galaxies $R_d \sim R_{25}/3.2$). The ratio $V_{\rm esc}/V_{\rm max}$ is, then, well below 2.5 for both galaxies, indicating that they may develop tidal tails during collisions. This is a comfortable confirmation, since both galaxies obviously have developed one or more tidal tails.

It is interesting to note that the inclinations of the seven tidal dwarf candidates lie between values of 50° and 65°, which are very similar to the inclinations of the progenitor galaxies, 59° and 66° for NGC 7319 and NGC 7318B, respectively (from the Lyon-Meudon Extragalactic Database, LEDA). If the candidate tidal dwarf galaxies are formed in the plane of the disks of the parent galaxies, they probably could keep the angular momentum of their progenitor disks. This inclination concordance would then be expected by virtue of the conservation of angular momentum of the system. However, the inclination found for the candidates could be biased by the fact that standard methods for deriving inclinations favor high values of inclination (low inclination values are harder to determine). In addition, since we do not have information on which side of the galaxy is pointing toward us, the two inclined disks with 60° inclinations could actually be separated by 120°!

4.6. *Summary of the Properties of the Tidal Dwarf Galaxy Candidates*

Table 4 summarizes the characteristics of each of the seven tidal dwarf candidates of Stephan's Quintet. A plus sign in an entry means in column (2) that the color is bluer than $B-R = 0.8$; in column (3) that SFR(Hα)/SFR(L_B) (see § 3.4) is typical of a tidal dwarf galaxy; in column (4) that if the galaxy presents a velocity gradient larger than 8.0 h_{75} km s^{-1} kpc^{-1} (this will be true for all the objects since they were classified as tidal dwarf candidates based on the presence of the velocity gradients); in column (5) that the mass of the galaxy as measured from the internal kinematics of the ionized gas is larger than the tidal mass obtained in § 4.1; and in column (6) that the escape velocity of the parent galaxy is lower than the velocity difference between the systemic velocity of the tidal dwarf candidate and that of the parent galaxy (assuming that the parent galaxy is NGC 7318B for all regions except for region 6, for which the parent galaxy is assumed to be NGC 7319). The last two columns of Table 4 indicate whether the candidate belongs to a tidal tail and if it is associated with an H I cloud.

Regions 6 and 21 seem to be those with the highest chance of surviving as single entities. This is especially true for region 6, where CO emission at the redshift and location of the galaxy has been recently detected (Gao & Xu 2000), indicating a molecular gas mass of a few times 10^8 $M_{\odot}$. Other less massive candidates such as regions 20, 22, and 23 may not be massive enough to become independent entities. However, we should keep in mind that the values for the mass were determined under the assumption that the regions are pure planar rotators, and hence these are lower limits. In fact, random motions of the gas and stars may provide significant dynamical support for the tidal dwarf galaxies, as indicated by their line widths. Larger values for the mass of the candidates (obtained if the internal dispersion velocity is also taken into account) would result in an increase in the number of objects that could survive.

Although the complex of regions 2–5 may not survive as a single entity (the tidal mass is very large, mainly because of the large radius of the complex), it may be split into several smaller candidates that could then survive the tidal forces exerted by NGC 7318B.

4.7. *Other Probable Tidal Dwarf Galaxy Candidates*

The H I map of Stephan's Quintet presented by Williams et al. (1999, their Fig. 5) shows that the H I component at velocity 6600–6700 km s^{-1} is distributed along a fragmented ring around the galaxy NGC 7319, possibly formed after a tidal interaction with NGC 7320C. Such H I rings have previously been observed in other interacting systems, such as NGC 5291 (Malphrus et al. 1997). The northwestern side of the H I ring overlaps the dwarf galaxy candidate identified as region 6. It is possible that there are other tidal dwarf galaxy candidates along what would be the continua-

tion of the ring, to the north, beyond region 6, north of NGC 7319, where H I is not measured by Williams et al.

Comparing the eastern side of the H I ring with an optical image of the Quintet, we note that the end of the tidal tail of NGC 7319 that points to NGC 7320C (in the southeastern side of the group) has a number of optical condensations (Hunsberger et al. 1996; Gallagher et al. 2000) that overlap with maxima in the H I distribution. These regions probably have velocities similar to that of the H I gas (6700 km s^{-1}) and are most likely tidal dwarf candidates formed during a past encounter between NGC 7319 and NGC 7320C. Other faint condensations can be seen in this region, between NGC 7319 and NGC 7320C. The velocities of these objects have to be measured in order to confirm their nature.

What is very intriguing at first is the exact superposition of the H I component at 6700 km s^{-1} with the galaxy NGC 7320, at 800 km s^{-1}. This superposition may be understood if the following is considered: Moles et al. (1998) noted that while in a narrowband image (e.g., Hα) NGC 7320 appeared symmetric, in a broadband image it appeared very asymmetric, showing an extension to its northwest. In fact, what may appear to be the northwestern extension of the nearby galaxy NGC 7320 in broadband images may be in reality a chain of smaller background objects (perhaps other tidal dwarf galaxy candidates?) superposed on the line of sight, but with velocities that coincide with that of the H I component at 6700 km s^{-1}. Other regions may have velocities of $\sim$5700 km s^{-1} (possibly associated with NGC 7318B). Support for this scenario comes from the mix of velocities measured in this region by Moles et al. (1998). Again, more velocity measurements of the condensations present in this region are needed.

Other tidal dwarf galaxies may be associated with NGC 7318A. Although Moles et al. (1998) did not consider this galaxy in the interacting history of the Quintet, it must have been part of collisions, given the peculiar pattern of dust seen in the *HST* image and because of the several linear features that seem to emanate from the galaxy. These are marked with arrows in Figure 1*c*. A few of these could be projected material from NGC 7318A into the intragroup medium, in the same way as has been observed for Arp 105 by Duc (1995). Alternatively, it could be material in the process of reaccretion onto the parent galaxy after an interaction. There seem to be two different types of linear features, a few that are long and filamentary, with very low surface brightnesses, and others that are small and have high surface brightnesses. Perhaps also region 6 may have been born out of gas from NGC 7318A and not from NGC 7319, as has been assumed throughout this paper. This would be an especially appealing scenario if we could confirm that there is material between galaxy NGC 7318A and region 6 at a common velocity (of $\sim$6700 km s^{-1}). However, it is more probable (see Fig. 2 of Xu et al. 1999) that the apparent optical connection between regions 8 and 4 (seen as a filament in the *HST* image) is at a lower velocity of 5900–6000 km s^{-1}. Also important would be to confirm whether the features marked in Figure 1*c* coincide with the velocity of NGC 7318A.

We would also like to point out that the emission detected in regions 7 and 9 and in the features between these two regions might be associated with the higher velocity component of the group at 6700 km s^{-1} instead of being related to the lower velocity component (as has been assumed in this paper). This is supported by the Hα – [N II] map presented by Xu et al. (1999, their Fig. 2), which shows clearly that these regions are dominated by emission from the high-velocity component. Further indirect evidence is their low Hα content despite their high optical luminosities (see Figs. 1*a* and 1*c*), which suggests that the emission from this area may perhaps fall at the very edge of the CFHT filter, where the transmission is minimum. These regions would not have been detected in the lower S/N data taken with the SAO 6 m telescope, where only very bright sources such as region 6 were detected. As can be seen from Figure 1*c*, the *optical* luminosities of the sources in the area between regions 7 and 9 are comparable to those of other regions identified by us. This only illustrates the incredible mixture of matter at two different velocities in this group.

4.8. *Properties of Region 6 in a Scenario Where NGC 7318A Is the Parent Galaxy*

We assumed in the previous sections that region 6 was formed from remnant gas from NGC 7319 (Moles et al. 1997). We favored this scenario based on the evidence from the H I observations (Fig. 5 of Williams et al. 1999), which showed a structure similar to a ring (an incomplete H I ring) around galaxy NGC 7319. The H I gas associated with region 6 seems to be part of this large ring, in which case region 6 would be formed from gas originally in NGC 7319. On the other hand, there is also the possibility that region 6 was formed from gas expelled from NGC 7318A. Support for this is given by Figure 1*c*, where linear features apparently associated with NGC 7318A are seen. In this scenario, region 6 might be located at the tip of a tidal tail that may originate at the northern arm of NGC 7318A. We need new velocity measurements of the region to decide between the two scenarios.

In the following, we give the parameters for region 6 in the case where it is physically associated with NGC 7318A: (1) it would be at a distance of 25 h_{75}^{-1} kpc from the parent galaxy; (2) it would have a tidal mass of 6×10^8 $M_\odot$, smaller than its inferred mass; (3) the difference between its radial velocity and that of the parent galaxy is still lower than the escape velocity of the parent galaxy; (4) its inclination ($60° \pm 15°$) would still be similar (within the errors) to that measured for the parent galaxy (49°, value taken from LEDA).

5. SUMMARY

We have presented *B* and *R* photometry and a Fabry-Pérot Hα map of 23 emission-line regions in Stephan's Quintet. All but one region may be associated with NGC 7318B (region 6 may be attached either to NGC 7319 or to NGC 7318A).

Our main results are as follows:

1. We find that seven of the regions have velocity gradients greater than 8 h_{75} km s^{-1} kpc^{-1}. We classify these as tidal dwarf galaxy candidates.
2. Two tidal dwarf candidates may be located at the edge of a tidal tail, one located within a tail, and for the four others there is no obvious stellar/gaseous bridge between them and the parent galaxy.
3. Two of the candidates are associated with H I clouds, one of which is, in addition, associated with a CO cloud.
4. The tidal dwarf candidates have low continuum fluxes and high Hα luminosity densities of $F(\mathrm{H}\alpha) = (1\text{–}60) \times$

10^{-14} ergs s^{-1} cm^{-2}, magnitudes of $M_B = -16.1$ to -12.6, sizes of typically $\sim 3.5\ h_{75}^{-1}$ kpc, $B-R$ colors between 0.3 and 1.3, gas velocity gradients of ~ 8–$26\ h_{75}$ km s^{-1} kpc^{-1}, SFR(Hα)/SFR(L_B) between ~ 1100 and 6000, masses of $\sim 2 \times 10^8$ to $10^{10}\ M_\odot$, and a median mass-to-light ratio of $7\ (M/L)_\odot$.

5. The lower limits on the masses of the candidate tidal dwarf galaxies determined from their rotation curves (assuming that they are pure rotators) are in two cases larger than their tidal masses.

6. Two of the seven candidates may have velocities such that they can escape the gravitational field of the parent galaxy.

7. Possible streaming motions within the tails may not have significantly affected the observed velocity gradients of those tidal dwarf candidates that are located within tails.

8. The dynamical criterion for formation of tidal tails during a collision, $V_{esc}/V_{max} < 2.5$, is followed by galaxies NGC 7319 and NGC 7318B.

A few of the tidal dwarf galaxies we identified in this study may survive as single entities, leading to the formation of new group members of Stephan's Quintet.

We would like to thank Jacques Boulesteix and the SAO staff (Professor V. Afanasiev, A. Burenkov, S. Dodonov, V. Vlasyuk, and S. Drabek) for their help during the observations. We would also like to thank S. Hunsberger, M. Marcelin, and Professor J. Sulentic for insightful discussions, and Lourdes Verdes-Montenegro for sending us the H I map of the Quintet. C. M. d. O. thanks the Observatoire de Marseille for their hospitality and funding of a trip in 1999 July. P. A. thanks the Brazilian funding agency FAPESP for the financial support for two visits to the Instituto Astronômico e Geofísico, projects 99/05514-3 and 99/03744-1. H. P. acknowledges the financial support of FAPESP through a postdoctoral position, project 96/06722-0, and the Mexican CONACYT under project 32303-E.

REFERENCES

Allen, R. J., & Sullivan, W. T., III. 1980, A&A, 84, 181
Amram, P., Balkowski, C., Boulesteix, J., Cayatte, V., Marcelin, M., & Sullivan, W. T., III. 1996, A&A, 310, 737
Amram, P., Boulesteix, J., Marcelin, M., Balkowski, C., Cayatte, V., & Sullivan, W. T., III. 1995, A&AS, 113, 35
Amram, P., Mendes de Oliveira, C., Boulesteix, J., & Balkowski, C. 1998, A&A, 330, 881
Arp, H. 1973, ApJ, 183, 411
Balkowski, C., Bottinelli, L., Chamaraux, P., Gouguenheim, L., & Heidmann, J. 1973, A&A, 25, 319
Bertin, E., & Arnouts, S. 1996, A&AS, 117, 393
Binney, J., & Tremaine, S. 1987, Galactic Dynamics (Princeton: Princeton Univ. Press)
Dubinski, J., Mihos, J. C., & Hernquist, L. 1999, ApJ, 526, 607
Duc, P.-A. 1995, Ph.D. thesis, Univ. Paris
Duc, P.-A., & Mirabel, I. F. 1998, A&A, 333, 813
Gallagher, J. S., III, Hunter, D. A., & Tutukov, A. V. 1984, ApJ, 284, 544
Gallagher, S. C., Hunsberger, S. D., Charlton, J. C., & Zaritsky, D. 2000, in ASP Conf. Ser. 211, Massive Stellar Clusters, ed. A. Lançon & C. Boily (San Francisco: ASP), 247
Gao, Y., & Xu, C. 2000, ApJ, 542, L83
Hibbard, J. E. & van Gorkom, J. H. 1996, AJ, 111, 655
Hickson, P., Mendes de Oliveira, C., Huchra, J. P., & Palumbo, G. G. C. 1992, ApJ, 399, 353
Hunsberger, S. D., Charlton, J. C., & Zaritsky, D. 1996, ApJ, 462, 50
Hunter, D. A., & Gallagher, J. S., III. 1986, PASP, 98, 5
Hunter, D. A., Hunsberger, S. D., & Roye, E. W. 2000, ApJ, 542, 137
Kron, R. G. 1980, ApJS, 43, 305
Landolt, A. U. 1992, AJ, 104, 340
Larson, R. B., & Tinsley, B. M. 1978, ApJ, 219, 46
Lequeux, J. 1983, A&A, 125, 394
Malphrus, B. K., Simpson, C. E., Gottesman, S. T., & Hawarden, T. G. 1997, AJ, 114, 1427
Mateo, M. 1998, ARA&A, 36, 435
Mayya, Y. D. 1994, AJ, 108, 1276
Moles, M., Márquez, I., & Sulentic, J. W. 1998, A&A, 334, 473
Moles, M., Sulentic, J. W., & Márquez, I. 1997, ApJ, 485, L69
Östlin, G., Amram, P., Masegosa, J., Bergvall, N., & Boulesteix, J. 1999, A&AS, 137, 419
Östlin, G., Amram, P., Masegosa, J., Bergvall, N., Boulesteix, J., & Marquez, I. 2000, A&A, submitted
Oort, J. H. 1965, in Stars and Stellar Systems, Vol. 5, Galactic Structure, ed. A. Blaauw & M. Schmidt (Chicago: Univ. Chicago Press), 455
Pierini, D. 1999, A&A, 352, 49
Plana, H., Boulesteix, J., Amram, P., Carignan, C., & Mendes de Oliveira, C. 1998, A&AS, 128, 75
Plana, H., Mendes de Oliveira, C., Amram, P., Bolte, M., Balkowski, C., & Boulesteix, J. 1999, ApJ, 516, L69
Sage, L. J., Salzer, J. J., Loose, H.-H., & Henkel, C. 1992, A&A, 265, 19
Shostak, G. S., Sullivan, W. T., III, & Allen, R. J. 1984, A&A, 139, 15
Williams, B. A., van Gorkom, J. H., Yun, M., & Verdes-Montenegro, L. 1999, in IAU Symp. 186, Galaxy Interactions at Low and High Redshift, ed. J. E. Barnes & D. B. Sanders (Dordrecht: Kluwer), 375
Xu, C., Sulentic, J. W., & Tuffs, R. 1999, ApJ, 512, 178
Zwicky, F. 1956, Ergeb. Exakten Naturwiss., 29, 344